Princeton Plasma Physics Laboratory

The role of annulus resonances in edge losses of wave-hearing power in cylindrical plasmas, and applications to NSTX

R. Perkins

January 2017

PRINCETON PLASMA PHYSICS LABORATORY

Princeton Plasma Physics Laboratory
Report Disclaimers

PPPL Report Availability

Princeton Plasma Physics Laboratory:

http://www.pppl.gov/techreports.cfm

Office of Scientific and Technical Information (OSTI):

http://www.osti.gov/scitech/

Related Links:

U.S. Department of Energy

U.S. Department of Energy Office of Science

U.S. Department of Energy Office of Fusion Energy Sciences

The role of annulus resonances in edge losses of wave-heating power in cylindrical plasmas, and applications to NSTX

R. J. Perkins and J.C. Hosea and N. Bertelli and G.Taylor and J. R. Wilson

Princeton Plasma Physics Laboratory, Princeton, NJ 08540

(Dated: December 22, 2016)

Abstract

Efficient high harmonic fast-wave (HHFW) heating on the National Spherical Torux eXperiment Upgrade would facilitate experiments in turbulence, transport, fast-ion studies, and more. However, previous HHFW operation on NSTX exhibited a large loss of fast-wave power to the divertor along scrape-off layer (SOL) field lines. It was postulated that the RF field amplitude is being enhanced in the SOL due to cavity-like modes, and that these enhanced fields are driving sheath losses through RF rectification. As part of ongoing work to confirm this hypothesis, we have developed a cylindrical cold-plasma model to identify and understand instances where a substantial fraction of wave power remains confined to the plasma periphery. We previously identified a peculiar class of modes, named annulus resonances, that conduct approximately half of their wave power in the periphery and can also account for a significant fraction of the total wave power. Here, we study the influence of annulus resonances on full three-dimensional reconstructions. We find instances where the annulus resonant modes dominate the specrum and trap over half of the total wave power in the edge. The work is part of an ongoing effort to determine the mechanism underyling these SOL losses on NSTX, identify optimal conditions for operation on NSTX-Upgrade, and check whether this mechanism could be present in future machines such as ITER.

I. INTRODUCTION

High-harmonic fast-wave (HHFW) heating is a promising heating scheme for the National Spherical Torus eXperiment Upgrade (NSTX-U). HHFW is complimentary to neutral beam injection in that it provides heating without particle or momentum input. Efficient fast-wave heating would enable a new generation of experiments on NSTX-U, including transport studies, low-rotation scenarios, and interacting with or even suppressing of fast-particle modes. Furthermore, as NSTX-U transitions to a high-Z metal wall in the upcoming years, HHFW may provide a crucial role in providing central RF heating, which has been shown on other machines to faciliate outerward impurity transport and avoid radiative collapse.

Unfortunately, previous experience with NSTX showed that efficient fast-wave heating was difficult to achieve in certain scenarios. Poor heating efficiency was observed for lower phasing and lower toroidal field [1, 2]. HHFW operation also improved with the lower SOL density provided by lithium deposition, provided that the machine was not vented to produce lithium compounds that proved very detrimental to HHFW performance [3]. That this lower heating efficiency is caused by SOL losses is evidenced by bright spirals that form in the upper and lower diveror [4] along field lines passing in front of the antenna [5]; infrared cameras measure a heat flux up to $2\,\mathrm{MW/m^2}$ under the spirals for an applied HHFW power of 1.8 MW. Given the parametric dependence of the losses, it was hypothesized that the losses are caused by significant fast-wave propagation was occuring in the SOL when the righthand cutoff layer, defined by $n_\parallel^2 = R$, with $n_\parallel$ the parallel refractive index and R the cold-plasma dielectric component from Stix notation, was positioned close to the antenna [2]. Subsequent conversion of HHFW power to the observed heat flux would occur through another process such as RF rectification [6]. Further support of this hypothesis was found in full-wave simulations of NSTX using the full-wave code AORSA [7] with the solution domain extended to include the SOL [8]. In a detailed scan of the SOL density in these simulations, the RF electric field amplitude grows to large values in the SOL when the SOL density is large enough that there is no cutoff region in front of the antenna [9]. It is important to note that there have been several instances of successful HHFW operation, including record-high T_e obtained from HHFW-only discharges[10], and plasmas that were 70% non-inductive [11], indicating that efficient heating is obtainable under the proper circumstances.

Motivated by these findings, we developed a cylindrical cold-plasma model to identify modes that carry significant wave power in the peripheral plasma. Such a model clearly lacks many details included in full-wave codes, but it provides a simplified framework the study the fundamentals of wave-propagation across a steep edge density gradient. We previously identified a peculiar class of modes, named "annulus resonances," that fit a half wavelength into the combined annulus/vacuum regions of the model. These modes have an enhanced loading resistance compared to other modes and propagate significant power in the edge. They are thus strong candidates to explain the edge losses on NSTX, and the present paper the influence of the annulus resonaces on three-dimensional reconstructions of the RF wavefields. This paper is structured as folows. Section II describes the model and the parameters chosen to represent NSTX discharges. In Sec. III, we explore properties of the annulus resonance with respect to m, the azimuthal mode number. We introduce families of modes, which appear as smooth curves in scatter plots of loading resistance and that clarify the behavior of the annulus resonant modes. In Sec. IV, the impact of the annulus resonance on the three-dimensional reconstruction is evaluated for a scan of the annulus density. The annulus-resonance condition forms a "ridge" in the $k_\parallel - k_\theta$ plane, which, by changing parameters such as the magnetic field, annulus density, and annulus width, moves relative to the peaks in the antenna spectrum. We find instances where the annulus resonant modes dominate the spectrum and leave over half the wave power trapped in the edge. We also find other instances where the role of the annulus resonant modes are less than dominant and core propagation in above 80%. That being said, the scaling of edge power percentage with plasma parameters obtained in the model do not always match observations, and Sec. V discusses the potential influence of field pitch in this discrepancy.

II. DESCRIPTION OF THE MODEL

The model geometry, illustrated in Fig. 1, consists of three radial regions: a core plasma, a lower-density annulus, and an outer vacuum region. The annulus region represents the SOL, and the vacuum region represents the extremely low density region behind the limiter and inside the antenna box. The core extends to radius r_c with constant density n_c. The annulus extends from $r = r_c$ to r_a with constant density n_a. The vacuum region extends from $r = r_a$ up to a conducting wall of radius r_w. The two-step density profile surrounded

by vacuum is a coarse approximation of the actual density but is partially justified on the basis that SOL density profiles are relatively steep near the separatrix but become nearly flat in the mid- to far-SOL [12, 13]. The perpendicular wavelength of the fast wave in the SOL is at smallest around 7 cm and is typically much larger; therefore, approximating a gradient of scale length 1 - 2 cm [14] is not obscene. A uniform axial magnetic field is used throughout. The use of a uniform magnetic field is partially justified since the focus of our study in on the SOL, over which the magnitude and direction of the magnetic field does not change appreciably, at least not as much as the density. The larger error comes in neglecting the poloidal field, which is substantial on NSTX. Field angles $\tan^{-1}(B_{\mathrm{pol}}/B_{\mathrm{tor}})$ up to 40° have been measured during HHFW experiments. The potential impact of this sizable tilt is discussed in Sec. V, but we note that large RF field amplitudes were observed in simulations using only a toroidal field [15]. The antenna is modelled as current straps carrying current in the θ direction at $r = r_s$ with a Faraday screen at $r = r_F$.
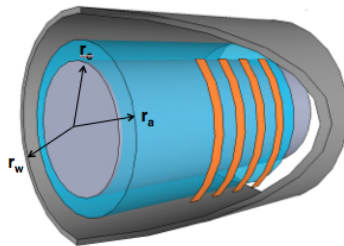

FIG. 1: Cartoon of the model showing the two-step density profile and orientiation of the antenna straps.

We chose values for the model parameters that resemble as much as possible NSTX discharges. For radii, we use a core radius of $r_c = 0.88$ m, an annulus outer radius of $r_a = 0.915$ m, a Faraday-screen radius of $r_F = 0.9315$ m, and a wall radius of $r_w = 0.9715$ m. The model core radius is chosen to keep the plasma cross-section area roughly the same as shot 120740, yielding an effective circular radius of 0.88 m. The annulus width $r_a - r_c$ chosen to be 3.5 cm based on average values of the experimental "outer gap" as determined from equilibrium magnetics for the L-mode discharges studied in Ref. [2]. The distance from the edge of the annulus to the Faraday screen is fixed at 1.65 cm, the distance between the outer boron nitride limiter and the Faraday screen at the midplane. The distances from the Faraday screen to the antenna strap is likewise fixed at ??, and from the antenna to the

vacuum wall at ??. $n_c = 5 \times 10^{19}$ m^{-3}, $f = 30$ MHz, $B = 0.32$ T (approximate field at the edge for a 0.55 T on-axis field).

A "mode" refers to a global solution which satisfies the wave equation in each region and which is matched at interfaces. Modes assume the form $\tilde{E}_z(r, m, k_\parallel) = \tilde{E}_z(r) \exp(im\theta + ik_\parallel z - i\omega t)$, based on Fourier analysis in the axial and azimuthal directions. With $k_\parallel$ given, $k_\perp$ is fixed in each region by the plasma regions by the cold-plasma dispersion: we use the notation $k_{\perp,c}^{\text{fast}}$ and $k_{\perp,c}^{\text{slow}}$ for the fast/slow wave $k_\perp$ in the core and corresponding notation $k_{\perp,a}^{\text{fast}}$ and $k_{\perp,a}^{\text{slow}}$ in the annulus. The slow-wave and vacuum $k_\perp$ are always cutoff. Radial RF field profiles are found by the method detailed in Ref. [16]. Each region admits four independent solutions. In plasma, there are two fast-wave solutions and two (cutoff) slow-wave solutions; in vacuum there are exponentially decaying and growing E_z (transverse magnetic) and H_z (transverse electric) modes. By specifying the boundary conditions are each interface, a system of equations is developed, whose simultaneous solution only exists when a determinant, denoted by the function $F(k_\parallel)$ vanishes, as described in Ref. [17]. As might be anticipated for oscillation in a bounded system, the roots of $F(k_\parallel)$ are such that an integral number of half wavelengths occur in the radial profile of E_θ. Thus, we can label modes with two numbers, (m, n), with m the azimuthal wavenumber and n the radial mode number. Because the fast-wave dispersion gives $k_\perp$ as a decreasing function of $k_\parallel$, lower n corresponds to larger $k_\parallel$.

The total fields are found by inverse Fourier transform:

$$E_\theta = \sum_m \int \tilde{E}_\theta(r, m, k_\parallel) \tilde{J}_{\text{ant}}(m, k_\parallel) e^{im\theta + ik_\parallel z} dk_\parallel, \tag{1}$$

The expression for $\tilde{E}_\theta$ contains $F(k_\parallel)$ in the denominator, so that the integral reduces to a sum of residues, one for each mode. In Eq. (1), $\tilde{J}_{\text{ant}}(m, k_\parallel)$ is the antenna spectral current density and $\tilde{E}_\theta$ the azimuthal electric field per unit antenna spectral current density. The amplitude of each mode is thus given by two factors: (i) the amplitude of $\tilde{J}_{\text{ant}}(m, k_\parallel)$ at the $k_\parallel$ and m of the mode, and (ii) the size of the residue, which is proportional to $(dF(k_\parallel)/dk_\parallel)^{-1}$. As described in Ref. [17], the large amplitude of an annulus resonance is due to a near vanishing of $dF(k_\parallel)/dk_\parallel$ independent of the particulars of the antenna configuration. Indeed, this paper describes the relative influence between antenna spectral weighting and "bare" mode amplitude in the relative strength of annulus resonances.

The antenna strap current distribution is modelled as twelve infinitely thin filaments. The

Fourier spectrum in the axial direction is therefore a sum of twelve plane waves. Given that the height of the antenna straps is 68.9 cm, and using the effective plasma radius above, we approximate the antenna angular span as 0.724 radians in the model. We assume a uniform current distribution in the azimuthal (poloidal) direction due to the long vacuum wavelength compared to the strap length. Given a phase difference of ϕ between straps, a strap spacing of d and the current of each I_0 and an angular span of α,

$$J_{\text{ant}}(r, \theta, z) = I_0 \delta(r - r_a) \left[\Theta(\theta + \alpha/2) - \Theta(\theta - \alpha/2)\right] \times$$
$$\sum_{i=0}^{12} \delta(z + (11 - 2i)d/2)e^{-i\phi(11-i)/2} \tag{2}$$

where Θ is a Heaviside step function. J_{ant} can be decomposed into a Fourier series in the azimuthal direction and a Fourier transform in the axial direction

$$\tilde{J}_{\text{ant}}(r, m, k_\parallel) = I_0 \delta(r - r_a) \tilde{J}_\theta(m) \tilde{J}_\parallel(k_\parallel) \tag{3}$$
$$\tilde{J}_\theta(m) = \frac{\sin(m\alpha/2)}{m\pi} \tag{4}$$
$$\tilde{J}_\parallel(k_\parallel) = \sum_{i=0}^{12} e^{ik_\parallel(11-2i)d/2} e^{-i\phi(11-i)/2} \tag{5}$$

We note that $\tilde{J}_\theta$ scales as $1/m$ and is nearly zero whenever $m\alpha/2$ is an integer multiple of π. This clearly favors low m modes. On the other hand, $\tilde{J}_\parallel$ is peaked around $k_\parallel = \phi/d$. For NSTX, $d = 21.5$ cm, and typically phasings are $\pi/6$, $\pi/2$ and $5\pi/6$. This model clearly ignores (i) the finite width of the antenna straps, (ii) the radial feeds [??], (iii) effects of sidewalls [18], and (iv) the change in current along the length of the straps.

In this paper, the term "mode amplitude" refers to the amount of wave power a mode conducts axially along the cylinder. We denote the amplitude of the (m, n) mode as $P_{m,n}$ but will also express this as a loading resistance $R_{m,n}$ defined by $R_{m,n}I_0^2/2 = P_{m,n}$, with I_0 defined in Eq. (2). $P_{m,n}$ can be calculated as the power output of the antenna, also refered to as the induced EMF method [19].

$$P_{m,n} = \int \left\langle \tilde{\mathbf{E}}(r, m, k_\parallel) \cdot \tilde{\mathbf{J}}_{\text{ant}}(m, k_\parallel)^* \right\rangle dV, \tag{6}$$

where $< \ldots >$ denotes time-averaging of complex quantities. Equivalently, $P_{m,n}$ can be computed by integrating the axial Poynting flux over the cross-section of the cylinder

$$P_{m,n} = \int_{r=0}^{r=r_w} \int_{\theta=0}^{\theta=2\pi} \hat{z} \cdot \left\langle \mathbf{E}(r, m, k_\parallel) \times \mathbf{H}(r, m, k_\parallel)^* \right\rangle r\,dr\,d\theta, \tag{7}$$

6

Equation 7 gives the same result regardless of the z position used to evaluate the integral, and both Eq. (6) and (7) yield the same result, as expected for a system without dissipation.

We emphasize that this cylindrical model is motivated by the need to qualitatively understanding and is not intended for precise calculations of loading resistances. The model is cylindrical, so toroidal effects are clearly excluded. The model does not include any of the surrounding the strap and Faraday screen; substantial reasearch has been done to study the effects of such components, especially when misaligned with the magnetic field and their possible excitation of an electric field component parallel to the background magnetic field. Finite-temperature and non-linear effects are omitted, including conversion to ion Bernstein waves, parametric decay instability, and RF rectification. Indeed, no form of dissipation is included; wave energy coupled from the antenna propagates out the ends of the cylinder without absorption. The mechanism converting HHFW power in the SOL to a divertor heat flux is not yet identified, but dissipation by far-field RF sheaths is a leading candidate [6]. Core absorption is the usual Landau damping and transit-time magnetic pumping. We presume that the high edge field amplitude of the annulus resonance will drive a high rate of edge absorption relative to core absorption once the proper SOL damping mechanism is identified and included, but this remains a crucial future step to verify. We also observe that this present model treats the tokamak as a plasma-filled waveguide, whereas the AORSA simulations including the SOL resemble more a plasma-filled cavity. We emphasize again that the cylindrical model allows for relatively rapid computation time and faster exploration of parameter space as well as the ability to resolve individual modes and separate the contribution between fast and slow waves.

III. PROPERTIES OF ANNULUS RESONANCES OVER SEVERAL AZIMUTHAL MODE NUMBERS

The annulus resonance condition is that a half-wavelength structure in E_θ fits into in the combined annulus/vacuum regions. The modes that most nearly satisfy this condition have a greatly enhanced loading resistance and propagate over half of their wave power in the edge. What we call "annulus resonant modes" are the mode, for each m, the most closely satisfies this condition and consequently has the largest loading resistance. Indeed, when the bare loading resistances for all modes of a single m are plotted against $k_\parallel$, the annulus

resonances, if present, appears as a peak in an otherwise monotonically decreasing curve, as shown in Fig. 2. "Bare" loading resistance means omitting the factor of $\tilde{J}_{ant}(m, k_\parallel)$ in Eq. (1); alternatively, it is the loading resistance calculated using a point-source antenna $J_{\mathrm{ant}}(\theta, z) = I_0\delta(z)\delta(\theta)$, which gives a uniform power spectrum. For the typical SOL parameters modelled here, one generally finds at most one annulus resonance per m. It is possible at there is no annulus resonance present, as shown in Fig. 2.
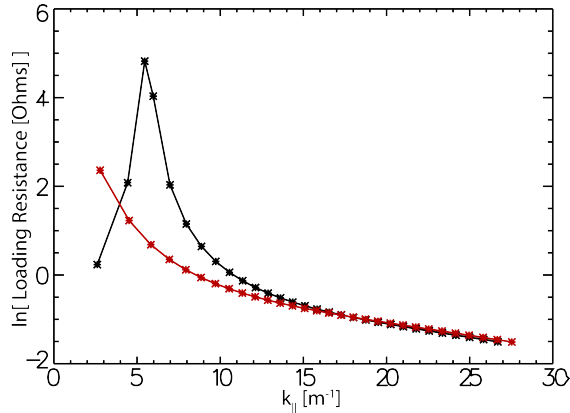

FIG. 2: Loading resistance for $m = 6$ (black) and $m = 0$ modes (red) for an annulus density of 1.5×10^{18} m^{-3}, showing typical behavior both with and without an annulus resonance.

This section will focus on the behavior of these modes for different m. As mentioned, there is typically at most one annulus resonance per m, but the $k_\parallel$ of the resonance increases with m. This is demonstrated in Fig. 3.a, where the bare loading resistance is plotted against $k_\parallel$ for select azimuthal mode numbers m. There is one annulus resonance for every m, and the $k_\parallel$-value of these peaks increases with increasing m. For low enough m (in this case, $m \leq 0$), this peak begins to disappear into the vacuum cutoff $k_\parallel = \omega/c$. In Fig. 3.b, the $k_\parallel$ value of the largest mode for each m is plotted against m; there appears to be a functional relationship. Figure 3.c is similar to Figure 3.b except the vertical axis is $k_{\perp,c}^{\mathrm{fast}}$, the fast wave $k_\perp$ in the core. This last plot appears piecewise linear with "breaks," consecutive modes that have similar $k_{\perp,c}^{\mathrm{fast}}$.

Figure 3.b is important to understand. The "trajectory" of the annulus resonance condition through $k_\parallel - m$ space determines whether or not these modes will intercept the peaks on the antenna spectrum. It is also important to understand how parameters such as magnetic field and annulus density effect this "trajectory."
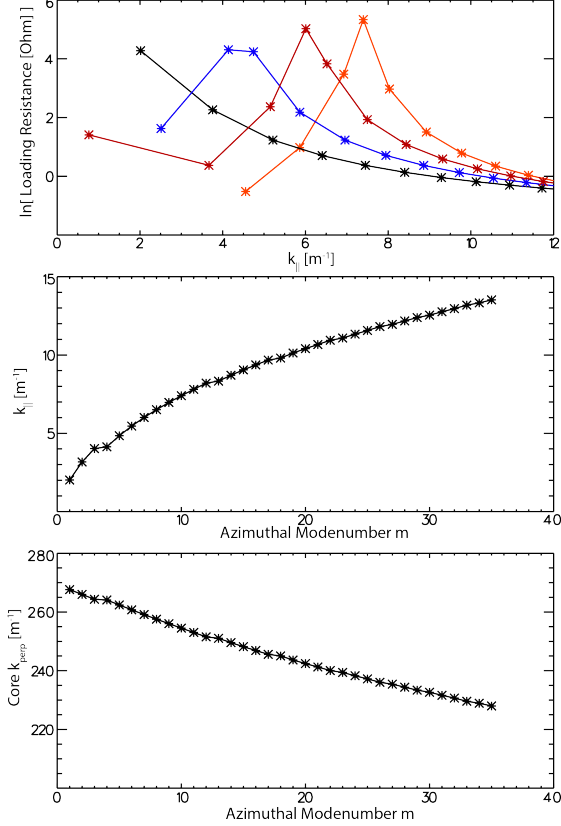
FIG. 3: *a) An overlay of loading resistance plots versus $k_\parallel$ for $m = 0$ to 8. For $m \geq 2$ a peak can be seen, corresponding to the annulus resonance. b) The $k_\parallel$ value of the largest mode for each m in (a) [e.g. the "annulus resonances"]. c) Similar to b) but with $k_{\perp,c}^{\mathrm{fast}}$ as the abscissa.*

A. Radial Mode Number n

The general behavior of the nth radial mode as a function of m can be roughly understood as follows. We introduce the change in wave phase across a radial region as

$$\delta\phi = \int_{r_0}^{r} k_\perp dr. \tag{8}$$

This borrows from the eikonal approximation. However, it is poorly defined, since in the vacuum region $k_\perp$ is imaginary, and also there can be abrupt changes in phase at the boundaries of regions. Nonetheless, this definition is useful, as will be shown. For the *nth* radial mode, the total phase change over the entire radial profile is πn. The vast majority of this phase change occurs over the core region as opposed to the combined annulus/vacuum region for two reasons: first, the higher core density greatly increases $k_\perp^{\mathrm{fast}}$

9

in the core relative to the annulus, and second the radius of the core is much larger than the width of the annulus/vacuum gap. To simplify notation, we will use the symbol ν to denote the fast-wave $k_\perp$, $k_{\perp,c}^{\text{fast}}$, and further let $\nu_{m,m}$ denote this value for the mth azimuthal mode and nth radial mode. The core fast wave fields are linear combinations of $J_m(\nu_{m,n}r)$ and $J_{m+1}(\nu_{m,n}r)$ and can be approximated by their asymptotic forms:

$$J_m(\nu_{m,n}r) \approx \sin\left(\nu_{m,n}r - m\frac{\pi}{2} - \frac{\pi}{4}\right), \tag{9}$$

so that we take the fast wave phase at the core-annulus boundary, denoted $\phi_{m,n}$ to be

$$\phi_{m,n} \approx \nu_{m,n}r - m\frac{\pi}{2} - \frac{\pi}{4} \tag{10}$$

Suppose we increase m by one but keep n fixed. With n fixed, the total fast wave phase across the entire radial profile is fixed, but since this is dominated by the phase across the core ($\phi_{m,n}$), we could say ϕ is approximately fixed. The factor $m\pi/2$ in Eq. (10) would tend to decrease ϕ with increasing m, so it follows $\nu_{m+1,n}r_c$ must be larger than $\nu_{m,n}r_c$ by approximately $\pi/2$:

$$\nu_{m+1,n}r_c \approx \nu_{m,n}r_c + \frac{\pi}{2}. \tag{11}$$

Increasing ν means decreasing $k_\parallel$. To test Eq. 11, Fig. 4 tracks the $n = 65$ mode from $m = 0$ to $m = 18$; for larger m, the annulus resonance disappears into the vacuum cutoff. The vertical axis is ϕ/π. For $m < 14$, the curve is very flat and nearly constant, which validates the above arguments and Eq. 11. As mentioned above, the deviation from flatness is likely due to the much smaller variation in phase across the annulus/vacuum regions (which is hard to quantify since the vacuum region and sometimes the annulus region are cutoff). At $m = 14$, there is an abrupt change in phase. For $m = 14$, the $n = 65$ mode is indeed an annulus resonance, and for larger m there is a node in the edge, explaining the abrupt change in phase in Fig. 4.

B. Mode Families

There appear to be families of modes whose loading resistances, when plotted against $k_\parallel$, lie on smooth curves that rise to a peak and then fall off into exponential decay. Figure 5a is a scatter plot of loading resistance versus $k_\parallel$ for all modes from $m = 0$ to $m = 40$. This is similar to Fig. 3 but on a logarithmic scale, with more azimuthal mode numbers, and no
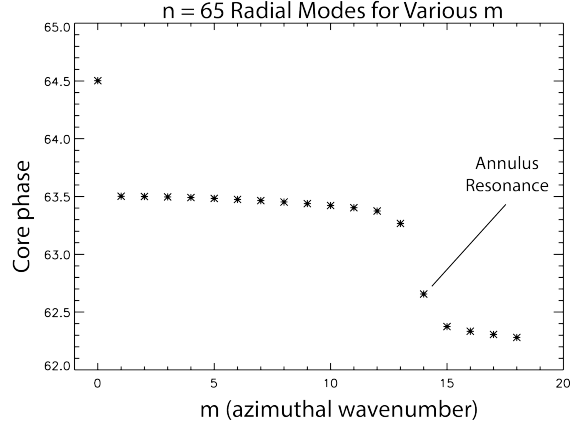
FIG. 4: *Core phase $\phi_{m,65}$ for the $n = 65$ radial mode, tracked over several m numbers.*

coloring to distinguish m. Figure 5 shows some structure: certain families of modes appear to lie on smooth curves that rise to a crest and then fall in amplitude with increasing $k_\parallel$. Figure 5b shows the same scatter plot with modes of the same m colored. With a given m, the modes jump across these smooth curve. Inspection of these smooth curves show that consecutive modes along the curve are obtained by increasing m by one and decreasing n by one, so that the sum $m+n$ is constant along any given curves. In Fig. 5c, modes with $m+n$ fixed are colored to differentiate different families. As one curve falls, another rises to take its place so that the crests of these curves defines an envelope curve, and annulus resonant modes are those modes that lie along this envelope. This feature is particularly emphasized by the $m = 4$ modes highlighted in Fig. 5b, where there is not one dominant mode but two closely spaced and nearly equal modes, each coming from a different family as the annulus resonance condition transitions from the $m + n = 77$ curve to the $m + n = 78$ curve.

Within a family of modes, the radial wavelength in the edge varies relatively slowly across modes. This is demonstrated in Fig. 6. In the lefthand column, m is held fixed at 6, but n is decreased by one from 73 (Fig. 6a) to 72 (Fig. 6b) to 71 (Fig. 6c). The width of the outermost half wavelength grows and sweeps across the annulus-core boundary, denoted by the dashed line at $r = 0.88$ m. The $n = 72$ mode most nearly satisfies the annulus resonance condition, and it correspondingly the largest mode. Increasing n by one to $n = 71$, the outermost wavelength is now larger than the edge width. In the righthand column of Fig. 6, however, we simultaneously decrease n by one and raise m by one, going from $m = 5$ and $n = 73$ (Fig. 6d) to $m = 6$ and $n = 72$ (Fig. 6e) to $m = 7$ and $n = 71$ (Fig. 6f). The width of the outermost wavelength now varies almost imperceptibly and remains close the
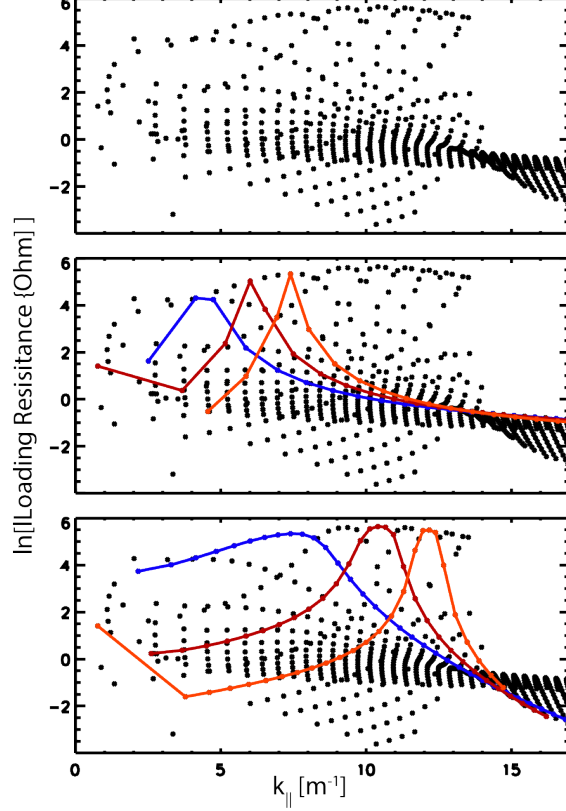
11

FIG. 5: (a) Scatter plot of all modes with $k_\parallel$ against the natural logarithm of loading resistance. Certain families of modes form smooth curves in this plot. (b) Scatter plot of all modes with the $m = 4$ modes highlighted red, highlighting the transition from one family to the next of the annulus resonance condition. (c) As in (a) with color and lines connecting all modes satisfying $m + n = $ constant.

annulus resonance condition. As one continues to increment m and decrement n keeping $m + n$ constant, the width of the outermost wavelength eventually growths larger than the edge width, losing the annulus resonance condition and leading to the fall off in mode amplitude. However, as the $m + n = 78$ family falls off, the $m + n = 79$ family begins to satisfy the annulus resonance condition more closely. It is currently not clear why holding $m + n$ constant slows the variation in the width of the outermost wavelength.

We can now reason out the dependence of $k_\parallel$ of the annulus resonance with m shown in Fig. **??**. Within a family, $m + n = $ constant. Using Eq. 11 and $\phi_{m,n+1} = \phi_{m,n} + \pi$, we get

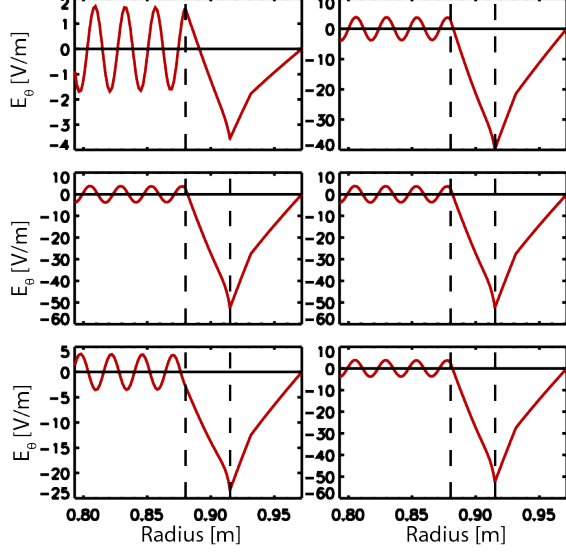$$\nu_{m+1,n-1} r_c = \nu_{m,n} r_c - \frac{\pi}{2}, \tag{12}$$

12

FIG. 6: Edge radial profiles of E_θ for various modes. In the left column, m is fixed at $m = 6$ while n is decreased by one moving down. In the right column, m is increased by one while n is decreased by one moving down.

form which the $k_\parallel$-dependence follows from the fast-wave dispersion:

$$n_\perp^2 = \frac{(R - n_\parallel^2)(L - n_\parallel^2)}{S - n_\parallel^2}. \tag{13}$$

Thus, increasing m within a family decreases ν but increases $k_\parallel$. Again, the smaller phase variation in the annulus/vacuum region will modify Eq. 12. Equation 12 is valid within a family and thus describes the behavior of the annulus resonance versus m over the $k_\parallel$ range for which this family has the dominant loading resistance. As mentioned above, though, the loading resistance of a particular family rises and falls while the next family rises. Thus, there are "transitions" or "handoffs" where we can expect a "break" in the m dependence of $k_\parallel$. This explains the piecewise linear behavior seen in Fig. 3.c.

To summarize the findings of this section, there is generally at most one annulus resonance per m, and the $k_\parallel$ value of this resonance increases with m in a predictable fashion.

IV.   THREE-DIMENSIONAL RECONSTRUCTIONS

In this section, we evaluate the role that AR modes play in full three-dimensional reconstruction of the wavefields. While the AR modes have a very large unweighted or "bare" loading resistance, if they do not coincide with the peak in the antenna spectrum, then

they will not be strongly excited. The dependence of $k_\parallel$ of the AR modes for different m studied in the previous section plays a central role: it defines the "trajectory" of the AR modes through the $k_\parallel - k_\theta$ plane and how closely it overlaps with the antenna spectral peak. This in turn determines how strongly the AR modes are excited in comparison with non-AR modes.

Section IV A, we introduce several useful concepts, including the amount of power that oscillates between the core and edge resions. Sections IV B and IV C present results for an inter-strap phasing of $\pi/2$ and $5\pi/6$ respectively. For several values of annulus density, we compute all the modes present in the system using a very inclusive m-range. While quantitative results are presented, the main emphasis is on the qualitatively behavior of the AR modes and in particular their location relative to the peaks in the antenna spectrum. We find instances where (i) the AR modes account for a large fraction of the total wave power, and (ii) a large fraction of the total wave power is "trapped" in the edge, as discussed in Sec. III. Indeed, the two features are fairly well-correlated, as expected. We have also found instances where the core loading is much better, and furthermore that the power in the edge can oscillate into the core. That being said, we find, in the case of $\pi/2$ antenna phasing, the *opposite* trending with annulus density with increasing annulus density, namely, in this model, power trapping in the edge tends to decrease with increased density. In the $5\pi/6$ phasing case, though, the power trapping is observed to increase initially with annulus density. We discuss the important role of magnetic pitch in Sec. V.

A. Power partition

We make some preliminary comments regarding the axial Poynting flux. The expression for the Poynting flux through a surface normal to the axial direction is

$$\langle S_z \rangle = \sum_{m,n,m',n'} \int \int \langle E_r(r,m,n) H_\theta^*(r,m',n') - \ldots$$
$$E_\theta(r,m,n) H_r^*(r,m',n') \rangle \, e^{i(k_\parallel - k'_\parallel)z + i(m-m')\theta} r \, dr \, d\theta,$$

from which we can appreciate that the presence of cross-terms leads to interefence between modes. If integration occurs over the entire azimuthal angle, then there is zero contribution unless $m = m'$. If integration occurs over the entire radial domain, then there is orthogonality of n and n'. In the case of both, then expression for axial wave power reduces to the

sum of individual fluxes from each mode with no interference between modes.

We consider the case where integration occurs over the entire azimuthal angle but not over the entire radial domain:

$$\langle S_z \rangle = 2\pi \sum_{m,n,n'} \int \langle E_r(r,m,n)H_\theta^*(r,m,n') - \ldots$$
$$E_\theta(r,m,n)H_r^*(r,m,n')\rangle\, e^{i(k_\parallel - k_\parallel')z}r\,dr$$

For each m, the sum over n and n' can be thought of as both diagonal terms ($n = n'$) and cross-terms ($n \neq n'$). The diagonal terms have no z-dependence, but the cross-terms do. If we take the region of integration to be the core, then the diagonal terms define a fixed amount of power that remains in the core, while the cross-terms define an oscillating power that can be added to and taken from the core and given to the edge. In general, the oscillating power consists of a number of terms which different beat wavelengths and must be computed numerically and each z-location of interest. A convenient and global metric of the total power available for oscillation can be obtained by

$$P_{osc} = 2\pi \sum_{n\neq n'} \int \langle E_r(r,m,n)H_\theta^*(r,m,n') - \ldots$$
$$E_\theta(r,m,n)H_r^*(r,m,n')\rangle\, r\,dr, \tag{14}$$

which is reminscent of an L^1-norm. Again, when considering the flux integrated from $\theta = 0$ to $\theta = 2\pi$, there is no oscillation of power between different m values. Also, if there is one dominant mode per m, then the amount of oscillating power can be expected to be a small fraction of the total wave power contained in these m-modes.

B. $\pi/2$-phasing: Current-drive phasing

The results of changing the annulus density in the range of 5.0×10^{17} m^{-3} to 2.0×10^{18} m^{-3} are summarized in Table I and shown graphically in Fig. 7. The general trend with increasing annulus density is that (i) total loading increases, (ii) the fractional loading to the core increases, and (iii) the percent contribution of the AR modes decreases. The increase in total loading results from increases in both AR and non-AR modes. The non-AR loading steadily increases with increasing annulus density, which improves core loading. Meanwhile the AR loading is not monotonically increasing for reasons discussed below, and contributes less to the total loading as n_a rises. We note that the amount of power that oscillates

15

Annulus	Loading				AR contribution		
Density	Total	Core (%)	Edge (%)	Oscillating	Core (%)	Edge (%)	Total (%)
0.5×10^{18}	2.37	1.60 (45%)	1.31 (55%)	0.24	14%	97%	62%
1.0×10^{18}	3.96	1.91 (48%)	2.04 (52%)	0.74	27%	94%	63%
1.5×10^{18}	3.93	2.68 (68%)	1.25 (32%)	0.85	23%	81%	42%
2.0×10^{18}	5.58	4.18 (75%)	1.41 (25%)	1.31	19%	76%	34%

TABLE I: Effect of increasing annulus density on the loading, and the role of the annulus resonant modes in each case. The lefthand columns show the total loading and its partition into edge and core power. Also noted is the amount of power that oscillates between core and edge. The righthand columns contain information about the AR modes. "Total" denotes the percent contribution of the AR modes to the total loading, while "Edge" and "Core" columns denote the percent contribution of the AR modes to the total loading in each region. For instance, 97% in the "Edge" column means that the edge power of the AR modes is 97% of the total edge power.
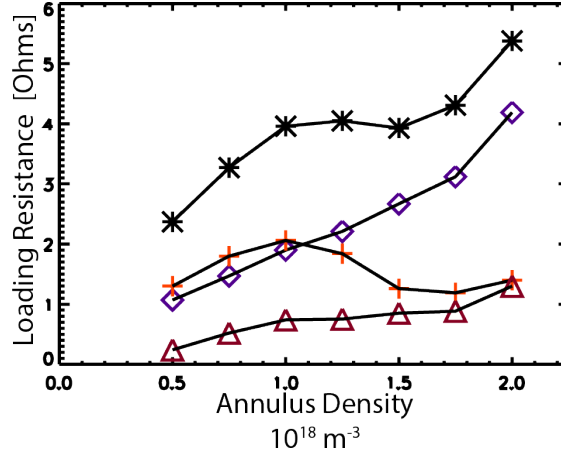

FIG. 7: Trend in loading resistance as annulus density is increased; stars: total loading, diamonds: core loading, plus: edge loading, triangles: oscillating power.

between the edge and the core steadily increases from a small fraction ($\sim 10\%$) to nearly the full power in the edge. We might say that the power in the edge is no longer trapped there. This is shown in Fig. 8, which plots the percentage in the core and edge as a function of z moving awaw from the antenna. In the low density case of $n_a = 5.0 \times 10^{17}$ m^{-3}, shown in Fig. 8a, the amount of oscillating power is small, and the amount of power in the edge is

16

close to its fixed value. In the case of $n_a = 2.0 \times 10^{18}$ m^{-3} shown in Fig. 8b, the overall power in the edge is lower, but a greater portion of it can oscillate into the core. Absorption is not included in this model, but with the relatively strong absorption predicted for NSTX-like plasmas, one may expect that any wave power that penetrates the core will be absorbed there.
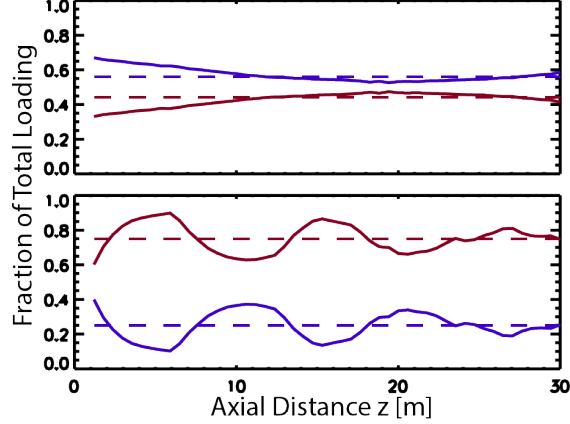

FIG. 8: Percentage of power contained in the core (red) and edge (blue) as a function of axial distance away from the antenna. Dashed lines indicated fixed percentage of power (Sec. IV A). (a) $n_a = 5.0 \times 10^{17}$ m^{-3}, and (b) $n_a = 2.0 \times 10^{18}$ m^{-3}.

A more detailed perspective is afforded by Figs. 9a and 9b. Each figure is a contour plot of the antenna spectral power plotted in the $k_\parallel - k_\theta$ plane, with each line denoting a factor of 2 drop/rise in spectral power. Each star denotes a mode, with lighter colors signifying a larger loading resistance. In these figures, only the largest fifty modes are plotted for clarity; this captures about 90% of the total wave power. The diamonds denote locations of the AR modes. These are plotted to show the trajectory of the AR trajectory and are plotted whether or not the AR is in the top fifty modes. That is, an empty diamond is an AR mode that is not in the top fifty modes. At an annulus density of 1.0×10^{18} m^{-1}, the AR ridge lies directly on top of the first azimuthal sideband, with $m = 12$ being the strongest AR mode excited. This explains the relatively strong contribution of the AR modes for this density. One can notice many non-AR modes on the primary antenna spectral peak. In Fig. 9b, the results of increasing the annulus density to 1.75×10^{18} m^{-3} moves the AR ridge off of the peak of the sideband. At the peak of the axial spectrum ($k_\parallel = 7.3$ m^{-1}), the AR ridge lies near the node in the azimuthal spectrum at $m = 8$. This explains the non-monotonic behavior in AR loading. Also, note that, for the strongest AR modes at the
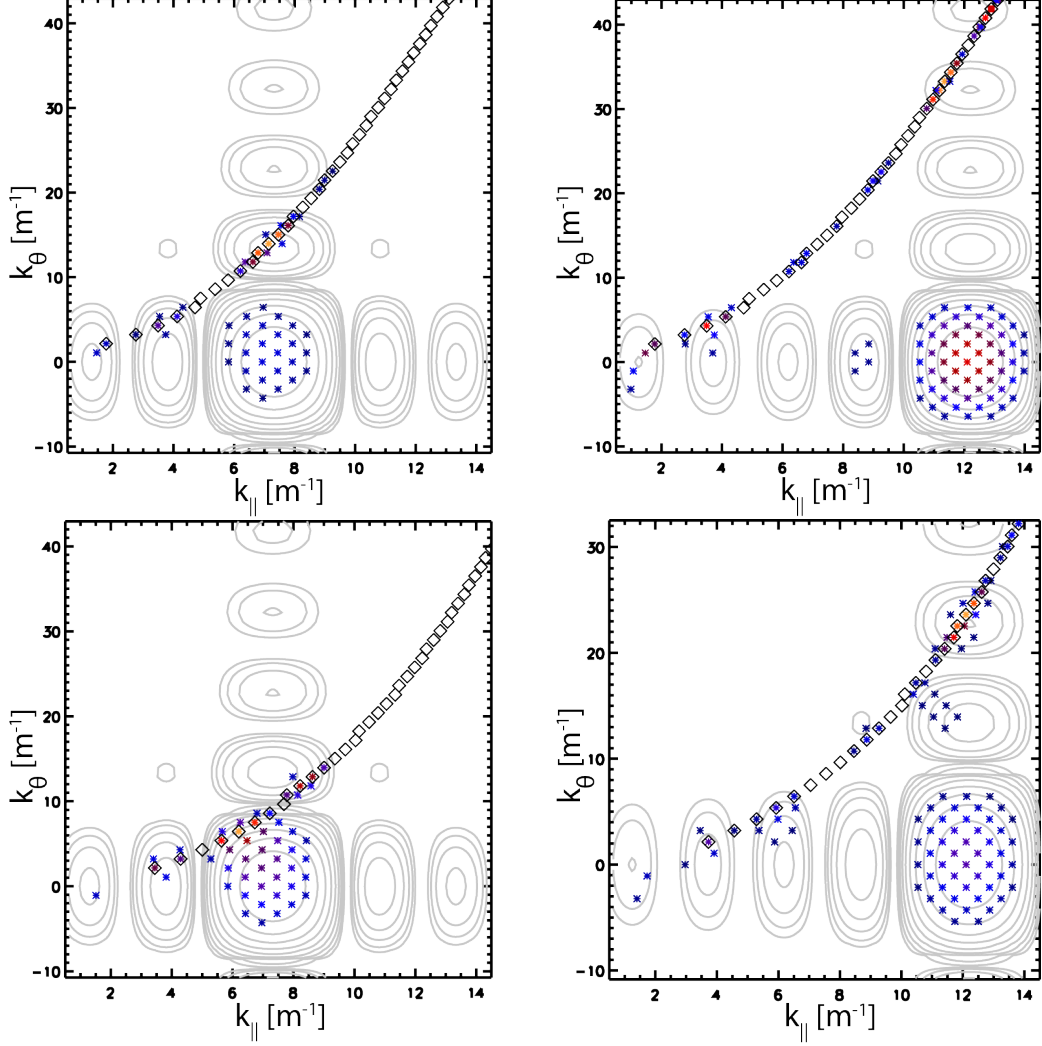
17

FIG. 9: Location of the AR ridge (diamonds) and top 100 modes (stars) relative to antenna spectral power (contour lines). (a) $pi/2$ phasing and $n_a = 1.0 \times 10^{18}$ m^{-3}, (b) $\pi/2$ phasing and $n_a = 1.75 \times 10^{18}$ m^{-3}, (c) $5\pi/6$ phasing and $n_a = 1.0 \times 10^{18}$ m^{-3}, (d) $5\pi/6$ phasing and $n_a = 2.0 \times 10^{18}$ m^{-3}.

$m = 5$, $m = 6$, and $m = 7$, neighboring modes of the same m are also strongly excited. With several large modes of the same m, the power oscillating between core and edge increases, as explained in Sec. IV A, this oscillation is caused by interference of modes of the same m. As evidenced in Fig. 9a, typically there is only one mode strongly excited at each m in the case of $n_a = 1.0 \times 10^{18}$ m^{-3}.

Also, for the entire set of AR modes, the fraction of power that they conduct in the edge decreases from $\sim 86\%$ power at $n_a = 5.0 \times 10^{17}$ m^{-3} to 56% at $n_a = 2.0 \times 10^{18}$ m^{-3}. This is

Annulus	Loading				AR contribution		
Density	Total	Core (%)	Edge (%)	Oscillating	Core (%)	Edge (%)	Total (%)
0.5×10^{18}	0.75	0.60 (81%)	0.14 (19%)	0.14	3%	97%	23%
1.0×10^{18}	1.10	0.75 (68%)	0.35 (32%)	???	8%	97%	36%
1.5×10^{18}	1.51	1.03 (68%)	0.48 (32%)	0.17	14%	93%	39%
2.0×10^{18}	2.16	1.46 (67%)	0.71 (33%)	0.35	18%	91%	42%

TABLE II: Effect of raising annulus density on both total loading and contribution from AR modes. Inter-strap phasing of $5\pi/6$

because higher-m AR modes conduct more power in the edge. Since the effect of increasing annulus density is to move the AR ridge to the right in $k_\parallel - k_\theta$ space, decreasing the m-value of the AR modes that lie over the antenna $k_\parallel$ peak.
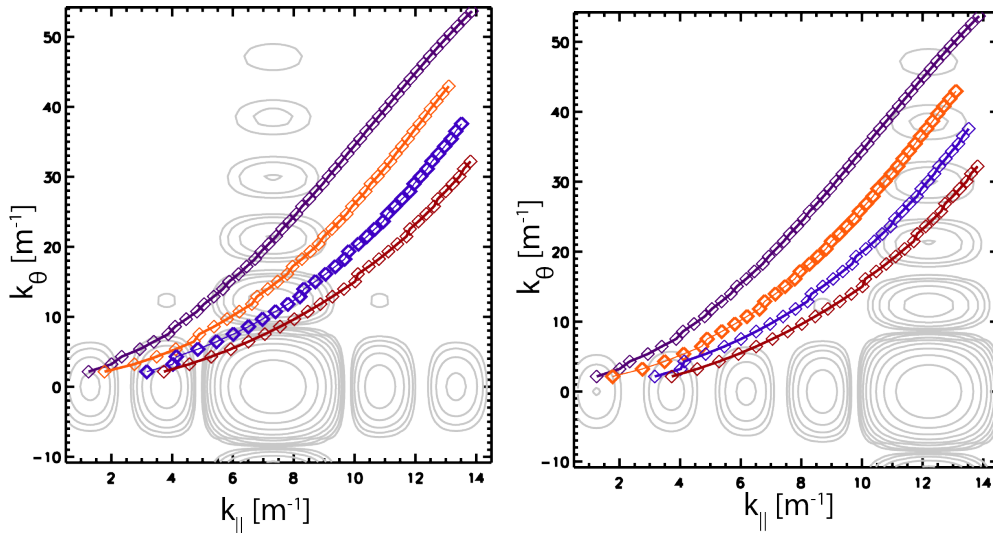

FIG. 10: Contour plot (black lines) of antenna spectral power and annulus resonances (diamonds) for different annulus densities. Changing the annulus density shifts the annulus resonance ridge relative to the antenna spectral peaks.

C. $5\pi/6$-phasing: Heating phasing

For this phasing, the axial spectrum peak increases to $k_\parallel = 12.2$ m^{-1}. This means that the AR that have a $k_\parallel$ matching the antenna need a higher m value, up to $m =$?? at

$n_a = 5.0 \times 10^{17}$ m^{-1}. Since the azimuthal spectral weighting of the antenna scales like m^{-2}, we may anticipate that the AR modes are not as strongly excited. Table II and Fig. **??** does indeed reflect this trend. The total loading is reduced and, as in the $\pi/2$ case, steady increases as the annulus density increases. However, both the percent loading to the edge and the contribution from AR modes rise as n_a is raised from 0.5 to 1.0×10^{18} m^{-1} but then level off in the range of 1.0 - 2.0×10^{18} m^{-1}. The edge loading as a function of n_a is steadily increasing, as opposed to its behavior for $\pi/2$ phasing.
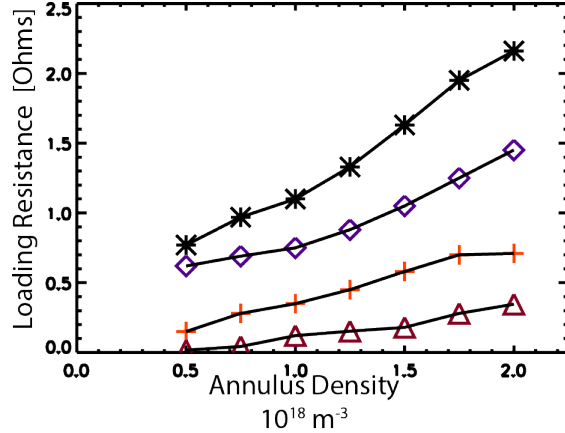

FIG. 11: Trend in loading resistance as annulus density is increased; stars: total loading, diamonds: core loading, plus: edge loading, triangles: oscillating power.

As shown in Fig. **??**, at an annulus density of 1.0×10^{18} m^{-3}, the strongest modes are the $m = 33$ and 34 modes, which lie over the third azimuthal sideband. The AR modes accout for 36% of the wave power, and the power in the edge is accordingly not too high, 32%. Also, at this phasing, the wave power is distributed over many modes; at $\pi/2$ phasing, 90% of the total power was carried by ~ 50 modes, whereas for $5\pi/6$ phasing it takes ~ 100 modes. As the annulus density is increased, there is again an increase in loading to non-AR modes, but the fractional increase is not as high as in the $\pi/2$ phasing case. However, the loading to AR modes greatly increases as the AR ridge intercepts $k_\parallel = 12$ m^{-1} at stronger azimuthal sidebands. Notice that the "slope" of the AR ridge at $k_\parallel = 12.2$ m^{-1} is greater than at $k_\parallel = 7.3$ m^{-1}, meaning the AR ridge is likely to cross two adjacent azimuthal sidebands and is less likely to lie in a null between them as in Fig. **??** of the $\pi/2$ case. At an annulus density of 2.0×10^{18} m^{-3}, the annulus-resonance ridge moves over the second angular sideband, giving relatively strong excitation of the $m = 21$, 22, and 23 AR modes.

This is remarkable, since the second angular sideband is ??? of the main peak, and yet the natural "bare" amplitude of the annulus resonance is large enough to make it the dominant mode. Increasing the density to 3e18 move the annulus resonance ridge over the first angular sideband, which increases both overall loading and also the percentage of power trapped in the edge.

V. DISCUSSION

The previous sections presented a conceptual framework that the annulus resonance modes form a ridge in the $k_\parallel - k_\theta$ plane, and that increasing the annulus density, for the current model parameters, moves this ridge line close to the peak in antenna spectrum.

In particular, the model predicts that the fraction of power coupled to the edge region decreases as the annulus density is raised. This contradicts operational experience [2] and also results from full-wave calculations [9].

We focus here on the potential role of field tilt of NSTX. Being a spherical torus, NSTX has a relatively weak toroidal field and a correspondingly large magnetic pitch at the outboard side, typically 30° to 40°. As a lowest order approximation to incorporate this pitch, one could rotate the projection of the k-vectors of the modes in the $k_z - k_\theta$ plane. Figure 12 shows how a rotation of 30° can move AR trajectory relative to the anntenna spectal peak for $5\pi/6$ phasing, and the effect is quite dramatic compared to the unrotated case of Fig. 10b. The rotated AR modes are decreased in k_θ, which would greatly increase their amplitude since the azimuthal spectal weighting scales as m^{-2}. Also, since the AR trajectory it is much more horizontal, we may expect a broad range of AR modes to be excited by axial sidebands of the antenna spectrum. While these speculations are based on a very coarse prescription of simply rotating k, it does suggest that field pitch could have a profound impact on the model.

VI. CONCLUSIONS

In a cylindrical magnetized cold-plasma model with a two-step density profile, there exists a special class of modes that have nearly a half wavelength in the combined annulus-vacuum regions, have a large loading resistance, and propagate over half their wave power in the
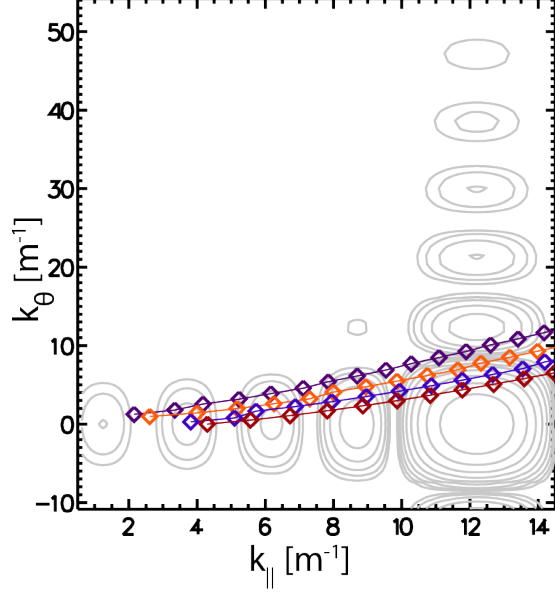
FIG. 12: Effect of a 30° rotation on the position of the annulus resonance ridge relative to the antenna spectral peaks for different densities: 0.5×10^{18} m^{-3} (purple), 1.0×10^{18} m^{-3} (orange), 1.5×10^{18} m^{-3} (blue), 2.0×10^{18} m^{-3} (red)

edge. There is typically at most one such mode per azimuthal modenumber m, and the $k_\parallel$ value of this mode increases with m. For the model parameters selected for this paper, the underlying reason behind this relationship between $k_\parallel$ and m is explained modes with the same $m+n$, with n the number of radial nodes, maintain the half wavelength condition over wide range of m. Viewed in the $k_\parallel - k_\theta$ plane, these modes line on a trajectory whose distance from the antenna spectral peaks changes with parameters such as annulus density. We have computed the relative contributions of AR and non-AR modes as well as the fractional loading to the edge and core regions over a scan of annulus density. As expected, edge loading is large when the AR modes contribute a substantial fraction to the total loading. We note cases where over half of the *total* wave power propagates in the edge with little flux of power between the edge and core. However, while total loading always increases with annulus density, the edge loading behaves non-monotonically for the $\pi/2$-phasing case, as the AR ridge moves onto and off of azimuthal sideband of the antenna spectrum. In the case of $\pi/2$ phasing, this leads to the results that the fraction of power coupled to the core improves with edge density, in contradiction to experiments and full-wave computations. The case of $5\pi/6$ phasing shows a degradation in core loading as annulus density increases in the range of $0.5 - 1.0 \times 10^{18}$ m^{-3} but levels off in the range $1.0 - 2.0 \times 10^{18}$ m^{-3}. Magnetic

pitch could play an important role; a coarse treatment indicates that rotating the k vectors of modes by the magnetic pitch at the antenna may bring the AR modes closer to the main spectral peak of the antenna, resulting in strong AR excitation.

[1] J. Hosea, R. Bell, S. Bernabei, L. DelgadoAparicio, B. LeBlanc, C. K. Phillips, P. Ryan, S. Sabbagh, K. Tritz, J. Wilgen, J. R. Wilson, and H. Yuh, "HHFW heating efficiency on NSTX versus B_ϕ and antenna $k_\parallel$," *AIP Conference Proceedings*, vol. 933, no. 1, pp. 107–110, 2007.

[2] J. Hosea, R. E. Bell, B. P. LeBlanc, C. K. Phillips, G. Taylor, E. Valeo, J. R. Wilson, E. F. Jaeger, P. M. Ryan, J. Wilgen, H. Yuh, F. Levinton, S. Sabbagh, K. Tritz, J. Parker, P. T. Bonoli, R. Harvey, and N. Team, "High harmonic fast wave heating efficiency enhancement and current drive at longer wavelength on the National Spherical Torus Experimental," *Phys. Plasmas*, vol. 15, no. 5, p. 056104, 2008.

[3] P. M. Ryan, R. Ellis, J. C. Hosea, C. C. Kung, B. P. LeBlanc, R. I. Pinsker, G. Taylor, and J. R. Wilson, "Operating the Upgraded NSTX HHFW Antenna Array In An Environment With Licoated Surfaces," *AIP Conference Proceedings*, vol. 1406, no. 1, pp. 101–104, 2011.

[4] J. C. Hosea, R. E. Bell, E. Feibush, R. W. Harvey, E. F. Jaeger, B. P. LeBlanc, R. Maingi, C. K. Phillips, L. Roquemore, P. M. Ryan, G. Taylor, K. Tritz, E. J. Valeo, J. Wilgen, J. R. Wilson, and the NSTX Team, "Recent fast wave coupling and heating studies on NSTX, with possible implications for ITER," *AIP Conference Proceedings*, vol. 1187, no. 1, pp. 105–112, 2009.

[5] R. J. Perkins, J. C. Hosea, G. J. Kramer, J.-W. Ahn, R. E. Bell, A. Diallo, S. Gerhardt, T. K. Gray, D. L. Green, E. F. Jaeger, M. A. Jaworski, B. P. LeBlanc, A. McLean, R. Maingi, C. K. Phillips, L. Roquemore, P. M. Ryan, S. Sabbagh, G. Taylor, and J. R. Wilson, "High-harmonic fast-wave power flow along magnetic field lines in the scrape-off layer of NSTX," *Phys. Rev. Lett.*, vol. 109, p. 045001, Jul 2012.

[6] R. J. Perkins, J. C. Hosea, M. A. Jaworski, J.-W. Ahn, A. Diallo, R. E. Bell, N. Bertelli, S. Gerhardt, T. K. Gray, G. J. Kramer, B. P. LeBlanc, A. McLean, C. K. Phillips, M. Podestà, L. Roquemore, S. Sabbagh, G. Taylor, and J. R. Wilson, "The contribution of radio-frequency rectification to field-aligned losses of high-harmonic fast wave power to the divertor in the

National Spherical Torus eXperiment," *Phys. Plasmas*, vol. 22, no. 4, 2015.

[7] E. F. Jaeger, L. A. Berry, E. F. DAzevedo, R. F. Barrett, S. D. Ahern, D. W. Swain, D. B. Batchelor, R. W. Harvey, J. R. Myra, D. A. DIppolito, C. K. Phillips, E. Valeo, D. N. Smithe, P. T. Bonoli, J. C. Wright, and M. Choi, "Simulation of high-power electromagnetic wave heating in the ITER burning plasma," *Phys. Plasmas*, vol. 15, no. 7, 2008.

[8] D. L. Green, L. A. Berry, G. Chen, P. M. Ryan, J. M. Canik, and E. F. Jaeger, "Predicting high harmonic ion cyclotron heating efficiency in tokamak plasmas," *Phys. Rev. Lett.*, vol. 107, p. 145001, Sep 2011.

[9] N. Bertelli, E. Jaeger, J. Hosea, C. Phillips, L. Berry, S. Gerhardt, D. Green, B. LeBlanc, R. Perkins, P. Ryan, G. Taylor, E. Valeo, and J. Wilson, "Full wave simulations of fast wave heating losses in the scrape-off layer of NSTX and NSTX-U," *Nuclear Fusion*, vol. 54, no. 8, p. 083004, 2014.

[10] G. Taylor, R. E. Bell, J. C. Hosea, B. P. LeBlanc, C. K. Phillips, M. Podestà, E. J. Valeo, J. R. Wilson, J.-W. Ahn, G. Chen, D. L. Green, E. F. Jaeger, R. Maingi, P. M. Ryan, J. B. Wilgen, W. W. Heidbrink, D. Liu, P. T. Bonoli, T. Brecht, M. Choi, and R. W. Harvey, "Advances in high-harmonic fast wave physics in the National Spherical Torus Experiment," *Phys. Plasmas*, vol. 17, no. 5, p. 056114, 2010.

[11] G. Taylor, J. C. Hosea, C. E. Kessel, B. P. LeBlanc, D. Mueller, C. K. Phillips, E. J. Valeo, J. R. Wilson, P. M. Ryan, P. T. Bonoli, J. C. Wright, and R. W. Harvey, "High non-inductive fraction H-mode discharges generated by high-harmonic fast wave heating and current drive in the National Spherical Torus Experiment," *Physics of Plasmas*, vol. 19, no. 4, p. 042501, 2012.

[12] B. LaBombard, R. L. Boivin, M. Greenwald, J. Hughes, B. Lipschultz, D. Mossessian, C. S. Pitcher, J. L. Terry, S. J. Zweben, and A. Group, "Particle transport in the scrape-off layer and its relationship to discharge density limit in Alcator C-mod," *Physics of Plasmas*, vol. 8, no. 5, pp. 2107–2117, 2001.

[13] J. A. Boedo, J. R. Myra, S. Zweben, R. Maingi, R. J. Maqueda, V. A. Soukhanovskii, J. W. Ahn, J. Canik, N. Crocker, D. A. D'Ippolito, R. Bell, H. Kugel, B. Leblanc, L. A. Roquemore, D. L. Rudakov, and the NSTX Team, "Edge transport studies in the edge and scrape-off layer of the National Spherical Torus Experiment with Langmuir probes," *Phys. Plasmas*, vol. 21, no. 4, p. 042309, 2014.

[14] S. J. Zweben, R. R. Myra, W. M. Davis, D. A. D'Ippolito, T. K. Gray, S. M. Kaye, B. P. LeBlanc, R. J. Maqueda, D. A. Russell, D. P. Stotler, and the NSTX-U Team, "Blob structure and motion in the edge of NSTX," *Plasma Phys. and Controlled Fusion*, vol. 58, p. 044007, 2016.

[15] N. Bertelli, E. Jaeger, J. Hosea, C. Phillips, L. Berry, P. Bonoli, S. Gerhardt, D. Green, B. LeBlanc, R. Perkins, C. Qin, R. Pinsker, R. Prater, P. Ryan, G. Taylor, E. Valeo, J. Wilson, J. Wright, and X. Zhang, "Full wave simulations of fast wave efficiency and power losses in the scrape-off layer of tokamak plasmas in mid/high harmonic and minority heating regimes," *Nuclear Fusion*, vol. 56, no. 1, p. 016019, 2016.

[16] W. P. Allis, S. J. Buchsbaum, and A. Bers, *Waves in anisotropic plasmas*, vol. 1. The MIT Press, 1963.

[17] R. J. Perkins, J. C. Hosea, N. Bertelli, G. Taylor, and J. R. Wilson, "Resonance in fast-wave amplitude in the periphery of cylindrical plasmas and application to edge losses of wave heating power in tokamaks," *Physics of Plasmas*, vol. 23, no. 7, p. 070702, 2016.

[18] V. Bobkov, D. Aguiam, M. Baruzzo, D. Borodin, I. Borodkina, S. Brezinsek, I. Coffey, L. Colas, A. Czarnecka, E. Delabie, P. Dumortier, F. Durodie, R. Dux, H. Faugel, H. Fnfgelder, C. Giroud, M. Goniche, J. Hobirk, A. Herrmann, J. Jacquot, P. Jacquet, A. Kallenbach, A. Krivska, C. Klepper, E. Lerche, S. Menmuir, D. Milanesio, R. Maggiora, I. Monakhov, F. Nave, R. Neu, J.-M. Noterdaeme, R. Ochoukov, T. Ptterich, M. Reinke, A. Tuccilo, O. Tudisco, D. V. Eester, Y. Wang, Q. Yang, and W. Zhang, "Progress in reducing ICRF-specific impurity release in ASDEX upgrade and JET," *Nuclear Materials and Energy*, pp. –, 2016.

[19] S. Ramo, J. R. Whinnery, and T. Van Duzer, *Fields and waves in communication electronics.* John Wiley & Sons, 2008.

Princeton Plasma Physics Laboratory
Office of Reports and Publications

Managed by
Princeton University

under contract with the
U.S. Department of Energy
(DE-AC02-09CH11466)